

REPORT DOCUMENTATION PAGE			Form Approved OMB No. 0704-0188	
Public reporting burden for this collection of information is estimated to average 1 hour per response, including the time for reviewing instructions, searching existing data sources, gathering and maintaining the data needed, and completing and reviewing the collection of information. Send comments regarding this burden estimate or any other aspect of this collection of information, including suggestions for reducing this burden, to Washington Headquarters Services, Directorate for Information Operations and Reports, 1215 Jefferson Davis Highway, Suite 1204, Arlington, VA 22202-4302, and to the Office of Management and Budget, Paperwork Reduction Project (0704-0188), Washington, DC 20503.				
1. AGENCY USE ONLY (Leave blank)	2. REPORT DATE 27.Oct.03	3. REPORT TYPE AND DATES COVERED MAJOR REPORT		
4. TITLE AND SUBTITLE "DETECTION AND DIAGNOSIS OF ORAL NEOPLASIA WITH AN OPTICAL COHERENCE MICROSCOPE"		5. FUNDING NUMBERS		
6. AUTHOR(S) MAJ CLARK ANNE L				
7. PERFORMING ORGANIZATION NAME(S) AND ADDRESS(ES) UNIVERSITY OF TEXAS AT AUSTIN		8. PERFORMING ORGANIZATION REPORT NUMBER CI02-1295		
9. SPONSORING/MONITORING AGENCY NAME(S) AND ADDRESS(ES) THE DEPARTMENT OF THE AIR FORCE AFIT/CIA, BLDG 125 2950 P STREET WPAFB OH 45433		10. SPONSORING/MONITORING AGENCY REPORT NUMBER		
11. SUPPLEMENTARY NOTES				
12a. DISTRIBUTION AVAILABILITY STATEMENT Unlimited distribution In Accordance With AFI 35-205/AFIT Sup 1		12b. DISTRIBUTION CODE		
13. ABSTRACT (Maximum 200 words)		DISTRIBUTION STATEMENT A Approved for Public Release Distribution Unlimited		
14. SUBJECT TERMS		15. NUMBER OF PAGES 35		
		16. PRICE CODE		
17. SECURITY CLASSIFICATION OF REPORT	18. SECURITY CLASSIFICATION OF THIS PAGE	19. SECURITY CLASSIFICATION OF ABSTRACT	20. LIMITATION OF ABSTRACT	

20031104 029

THE VIEWS EXPRESSED IN THIS ARTICLE ARE THOSE OF
THE AUTHOR AND DO NOT REFLECT THE OFFICIAL
POLICY OR POSITION OF THE UNITED STATES AIR
FORCE, DEPARTMENT OF DEFENSE, OR THE U.S.
GOVERNMENT

***Detection and Diagnosis of Oral Neoplasia with an
Optical Coherence Microscope***

A. L. Clark¹, A. Gillenwater², R. Alizadeh-Naderi², A. K. El-Naggar²,

R. Richards-Kortum¹

¹Department of Biomedical Engineering, University of Texas at Austin, TX, USA

²Departments of Head and Neck Surgery and Pathology, The University of Texas M.D.

Anderson Cancer Center, Houston, TX, USA

Research Support

This research was supported by the National Institutes of Health (Grant #1 RO1 CA 82880-01).

Corresponding Author

Dr. Rebecca Richards-Kortum

Department of Biomedical Engineering

The University of Texas at Austin

Austin, Texas 78712

Work: (512) 471 – 2104

Fax: (512) 471 – 0616

E-mail: kortum@mail.utexas.edu

Introduction

Optical coherence microscopy (OCM) is a new optical imaging technology that can provide detailed images of tissue architecture and cellular morphology of living tissue. The technique combines the sub-cellular resolution of high numerical aperture (NA) confocal microscopy with the increased sensitivity and penetration depth of optical coherence tomography (OCT) to acquire detail similar to that available in histologic tissue evaluation, except that images can be achieved non-invasively and without the need for fixation and histochemical staining. OCM images have been acquired from biological structures, with a resolution of 2 microns [1] a 200 – 500 micron field of view at a penetration depth of 600 microns in plant specimens [2, 3] and *in vitro* human colon tissue [4]. Thus, OCM provides the potential to image epithelial tissue with the subcellular resolution needed to assess the pathologic state of tissue.

OCM imaging builds detailed images of cell morphology and tissue architecture by using a high numerical aperture (NA) confocal microscope to collect light backscattered by various tissue components to provide contrast. The high NA objective focuses light to a three-dimensional voxel within the tissue and a pinhole placed at a conjugate image plane within the confocal microscope allows light reflected from the focal volume to pass to the detector, while most light generated from out of focus points is blocked. Further rejection of out of focus light is achieved by using an interferometric gate to reject those photons that pass through the pinhole, but have not traveled the same optical pathlength as light generated at the focal volume which has not undergone any further scattering events before exiting the tissue [1, 5]. Changes in refractive index provide a source of reflected light at the image point, and the contrast necessary to recognize intracellular detail. At this time, OCM imaging has been limited to relatively few

biological tissues, but results from confocal microscopy and OCT support the potential of both optical modalities for imaging lesions in epithelial tissue.

Both confocal microscopy and OCT have had success in visualizing pre-cancerous and cancerous conditions. High NA confocal microscopy with its subcellular resolution enables imaging of cell morphologic and tissue architectural changes associated with dysplasia and cancer. In skin, where cytoplasmic melanin provides a strong source of backscattering, confocal microscopes have captured morphologic changes in cytologic structure and visualized microvasculature in both basal cell carcinomas and melanomas [6-9]. In amelanotic epithelial tissues, where cell nuclei provide the primary source of reflected light, recent work showed that reflectance confocal imaging of normal and precancerous cervical tissue can characterize nuclear size, nuclear density and nuclear to cytoplasmic ratio without the need for tissue sectioning or staining. Parameters extracted from confocal images could be used to discriminate high grade cervical precancers with a sensitivity of 100% and a specificity of 91% in a study of 25 samples [10]. In a study of the esophagus [11], nuclear to cytoplasmic ratios were extracted from confocal images of normal esophagus and esophageal cancer; differences were statistically significant and could be used to identify cancer with a diagnostic accuracy of 90%. Confocal imaging of oral mucosa has resolved subcellular detail at depths of 250 microns and 500 microns in the lip and tongue, respectively [12], and captured many features of normal mucosa and oral squamous cell carcinoma from multiple sites within the oral cavity [13].

While high resolution OCT imaging has demonstrated resolution on the order of 1 micron [14], current clinically tested OCT systems do not provide images with the subcellular resolution characteristic of high NA reflectance confocal microscopy. They are able to use the penetration

depth capability of up to 1 mm to resolve architectural differences associated with the epithelial and stromal layers as precancers and cancers develop. In a study of the cervix, an OCT system captured irregularities in the epithelial layer and basement membranes of carcinoma in situ as well as lack of definition in the basement membrane associated with invasive carcinoma [15]. OCT endoscopes have also successfully imaged a large number of internal sites. These systems demonstrated a reduction in the distinction between epithelial and stromal layers in OCT images of precancerous and cancerous tissues of the larynx, esophagus, uterine cervix, colon, urinary bladder and esophagus [16-22] when compared to normal tissue.

The goal of this study was to characterize the features of normal and neoplastic oral mucosa using OCM and to compare these to the image features available with confocal microscopy. We report results of a pilot study using both a confocal microscopy and an OCM system to image pairs of clinically normal and abnormal biopsies obtained from 12 patients. We find that, like confocal microscopy, OCM can image oral mucosa with resolution comparable to histology without the need for tissue fixation, sectioning or staining. In addition to subcellular resolution, the OCM demonstrated consistently deeper penetration depths than achieved by the confocal arm of the system. Analysis of epithelial scattering coefficients clearly discerns a difference between the hyperkeratotic layers and the non-keratinized epithelium below and an increase in scattering associated with premalignancy.

Methods and Materials

Specimens

Oral cavity biopsies were acquired from 12 patients at the Head and Neck Clinic of the University of Texas M. D. Anderson Cancer Center who were undergoing surgery for squamous cell carcinoma (SCC) within the oral cavity. Informed consent was given by all patients, and the project was reviewed and approved by the University of Texas M. D. Anderson Cancer Center Office of Protocol Research and the Institutional Review Board at the University of Texas at Austin. Biopsies (approximately 3 mm wide by 4 mm long by 2 mm thick) were acquired from at least one clinically normal appearing and clinically suspicious area and immediately placed in growth medium (DMEM, no phenol red). Both optical coherence and reflectance confocal images were obtained at multiple image plane depths from the biopsies within twelve hours of excision. Following imaging, biopsies were fixed in 10% formalin and submitted for routine histologic examination by an experienced head and neck pathologist. Additional sections from four of the biopsies were stained with Monoclonal Mouse anti-Cytokeratin (Pan) (MMAC) Concentrate Antibody (Zymed Laboratories, Inc.), a broad spectrum monoclonal antibody cocktail of clones A1 and A3 which reacts to cytokeratins 10, 14/15, 16 and 19 in the acidic subfamily and all members of the basic subfamily, to assess correlations between confocal image features and the presence of keratin in the specimen.

Optical Coherence System

Images were obtained from each biopsy using an OCM system (Fig. 1). Illumination was provided by a broadband superluminescent diode (Superlum Diodes, Ltd., SLD 38) operating at

850 nm with a 25 nm full-width half maximum (FWHM) bandwidth and delivered to the confocal microscope through a 50/50 coupler and a single-mode optical fiber. The illumination light was collimated to a beam diameter of 8 mm upon exciting the optical fiber and delivered to a water immersion microscope objective (40X, 0.8 NA) via a raster-scanning system. This scanning system used a resonant scanner providing an 85 Hz line scan rate and a slow scan galvanometer to move the focused light in the sample, allowing acquisition of images in 3 seconds. The objective focused light to a 1 micron-diameter spot with an average illumination power of 0.4 mW. Light backscattered from the tissue was recoupled into the optical fiber, mixed in the 50/50 coupler with light returning from a reference arm and sent to a low-noise, broadband detector (New Focus, 1801-FC).

If the pathlengths of light returning from the sample and reference arm matched to within a coherence length of the SLD, interference fringes were produced at the detector. The pathlength of the reference light was small-amplitude (<1 micron) modulated using a technique described in [23, 24] where light was reflected from a mirror mounted on a sinusoidally driven piezo (NEC, AE0203D04). Demodulation of the first two harmonics of this modulated signal allowed reduction and even elimination of variation in the signal caused by thermal drifts in the pathlengths of the reference and sample optical fibers [4]. Hoeling demonstrated that the thermal variation could be eliminated if a modulation frequency of 122 kHz was used [23], but in order to raise our image acquisition rate, we increased our modulation frequency to a resonant frequency at 376.65 kHz. At this higher frequency, the displacement of the mounted piezo per volt was too low to balance the two harmonics without damage to the piezo, but a driving signal of $7.5 V_{p-p}$ was used to provide a peak-to-peak displacement of 315 nm and 65% reduction in

phase variations. The resulting signal was amplified by 26 dB and bandpass filtered to isolate the two harmonics and reduce noise. A RMS detector (Analog, AD8361) demodulated the signal and provided an estimate of signal intensity, or the square of the fringe amplitude. A complementary estimate of signal intensity was acquired by blocking the reference arm illumination and measuring the intensity of the backscattered light returned from the confocal microscope. This confocal signal returned to the computer through a separate electrical path which bandpass filtered the signal to 250 kHz and provided 10 dB of amplification.

The OCM system operated at a dimensionless fiber spot size, A , [25] of 2.81 to optimize optical sectioning. The measured lateral and axial resolution of the system were 2.3 microns and 7.8 microns, respectively. The field of view was adjustable from 150 – 250 microns by controlling the deflection of the scan mirrors.

Imaging and Image Processing

Prior to imaging, the biopsies were removed from growth media, rinsed with phosphate buffered solution (PBS), and oriented so the image plane of the microscope was parallel to the epithelial surface and would approach the epithelial layer first. A 6% solution of acetic acid was then added to each sample to increase image contrast [26]. OCM and confocal image pairs were acquired at various epithelial depths until tissue details were no longer resolvable by either of the imaging modalities. Upon acquisition, image voltage data was saved to a file as floating point numbers and also translated into 8-bit, grayscale format using a full-scale contrast stretch algorithm to produce individual images. Each of the image frames presented here were given additional post-processing to increase image quality. Brightness was enhanced by adding a

selected percentage of full gray scale to each pixel and contrast increased by removing another percentage of full gray scale from the image and expanding the remaining midrange gray levels.

Images of stained histologic sections were acquired using a color CCD camera coupled to a brightfield microscope. The small field of view of the OCM made it difficult to register exactly where in the biopsy images were acquired; in each case we identified areas in histologic sections that corresponded to features present in our images.

Scattering Coefficient Analysis

A selection of image depth of focus stacks were also processed to estimate the epithelial tissue scattering coefficient using a technique described in [27]. An estimate of the aggregate tissue scattering coefficient can be calculated using the equation,

$$I(z) = I_0 e^{-\mu_t z} R(z) e^{-\mu_t z} = I_0 e^{-2\mu_t z} R(z) \quad (1)$$

where I_0 is the incident intensity, $R(z)$ is the depth dependent reflectivity, and μ_t is the attenuation coefficient, which is the sum of the absorption and scattering coefficients. This technique assumes that excitation and reflected light travels parallel to the optical axis and that the attenuation coefficient does not vary as a function of depth. In the near infrared, where we made our measurements, the absorption coefficient is significantly lower than the scattering coefficient [28] so the attenuation coefficient was assumed to equal the scattering coefficient. Binary masks outlining nuclei were hand-segmented by one person using a graphics editing program (JASC, Paintshop). A mean reflected intensity for these nuclei was calculated using the nuclear masks to extract specific voltage levels from the detector values saved during imaging and plotted as a function of depth for each stack. These data were fit to (1) by minimizing the

mean square error between the data and the fit with the scattering coefficient as the only variable parameter.

Results

Imaging Results

Both OCM and confocal images were successfully obtained from 28 biopsies acquired from 12 patients with resolution similar to that provided by bright-field microscopy typically used to examine histologic sections. Table 1 shows the number of clinically normal and abnormal specimens obtained from each site within the oral cavity. Table 2 lists the histopathologic diagnoses for each biopsy from each patient with 20 showing hyperkeratosis, 14 exhibiting hyperplasia, four with mild dysplasia (two focal), three with moderate dysplasia (one focal), one with focal severe dysplasia, one moderately differentiated squamous cell carcinoma (SCC), one well differentiated SCC, and three specimens having no diagnosis due to a lack of epithelium in the histologic section.

OCM images were acquired by scanning focused light in a plane parallel to the epithelial surface. Figure 2F shows a histology image from a biopsy with hyperkeratosis and hyperplasia from the floor of the mouth, flanked by confocal (Fig. 2A – E) and OCM (Fig. 2G – K) images taken from the same biopsy at the different depths indicated by the lines on Fig.2F. Images from the superficial epithelium (Fig.2A, B, G, and H) taken at 50 and 150 microns beneath the epithelial surface show larger cells with extensive keratin providing bright return from the cell periphery regions while those acquired from 250 microns below the tissue surface (Fig. 2C and I) capture the more uniform, smaller cells associated with the intermediate layer. The images from

the basal epithelium at 300 microns below the tissue surface (Fig. 2D and J) visualize a distinct increase in cell density and nuclear to cytoplasmic ratio, but contrast in the confocal image (Fig. 2D) is now significantly reduced. At this depth, the OCM is still able to resolve cell membranes (arrow) (Fig. 2J) and at 350 microns below the tissue surface (Fig. 2K), basal cells are still visible in one portion of the image (arrow) while areas of low return represent where part of the image plane has traversed the basement membrane into stroma (double arrows). Confocal and OCM image features compare well with the corresponding transverse histologic section (Fig. 2F). This pattern of confocal and OCM images was typical of those recorded from normal biopsies in this study.

Detection of oral dysplasia requires sub-cellular resolution to capture changes in nuclear shape and area characteristic of pathologic changes in tissue during pre-malignant progression. Figure 3 shows both histologic and OCM images from a hyperplastic and hyperkeratotic biopsy from gingiva (A, C) and an invasive, well differentiated squamous cell carcinoma from the soft palate (B, D). The nuclei in Fig. 3A and Fig. 3C demonstrate the consistent shape, area, and spacing common to healthy tissue. In sharp contrast, the tightly packed tumor cells imaged in Fig. 3B and Fig. 3D exhibit extensive variations in nuclear size and nuclear morphology. Epithelial nuclei (single arrows) appear as bright areas on the OCM image, whereas areas of stroma with inflammation (double arrows) appear dark in the OCM image.

Penetration Depth and Scattering Coefficient Analysis

An important performance measure for optical imaging in tissue is the maximum depth at which images can be obtained, or the penetration depth. Imaging performance for both modalities was analyzed for the 23 biopsies in which consistent features were resolved

throughout imaging. For this analysis, penetration depth was defined as the maximum depth at which imaging captured individual nuclei. The results of this analysis are shown in Figure 4. The OCM consistently imaged more deeply than the confocal microscope, imaging 100 or more microns deeper than confocal microscopy in 3 cases, 50 microns or more in 7 cases, and less than 50 microns deeper in 13 cases. Overall, the penetration depth of the OCM exceeded the penetration depth of the confocal by an average of 33%. The widely divergent penetration depths for the study (93 – 338 microns for the OCM) illustrate the challenge presented by the diversity of tissue types and pathologic states found in the oral cavity.

An analysis of epithelial scattering coefficients for these samples was also performed. Twenty-nine depth of focus stacks, representing 16 biopsies, were selected. Stacks were chosen based on clarity of nuclei over at least 5 image depths and a maximum of two stacks per biopsy were used. In 23 of 29 stacks, an exponential curve could not be fit to the entire reflected nuclear intensity curve because a region existed at the beginning of the data that did not fit the model. Reflectivities in these regions varied greatly with signal commonly increasing during the first 20 – 50 microns, before either remaining relatively constant or dropping off significantly. In 14 of the 23 stacks, the signal started to attenuate exponentially at a specific depth. Upon examination of the pathology diagnosis for these cases, it became apparent that all 23 of these samples came from hyperkeratotic biopsies while three of the remaining six stacks were SCCs without hyperkeratotic layers and another two came from a biopsy with a very minimal hyperkeratotic layer. Figure 5 shows two examples of the reflected nuclear intensity versus depth; the hyperkeratotic layers are clearly distinguishable in both the histology and the normalized nuclear reflectance plots. Figure 5A shows a histologic image from a keratin

antibody (MMAC) stained section from a hyperkeratotic and hyperplastic gingiva biopsy with a plot of normalized reflected nuclear intensity taken from the same biopsy (Fig. 5B). The top 10 – 20 microns of the biopsy are heavily keratinized followed by a 40 – 90 micron layer of keratinized cells. This layer is recorded in the plot by a brief period of increasing reflected nuclear intensity before the signal becomes relatively constant until 70 microns below the tissue surface. At this depth, the intensity begins to drop. When the data from 70 – 150 microns is fitted to an exponential curve, the fit constant is 54 (with a R^2 value of 0.91), implying a scattering coefficient of 27 cm^{-1} . The histologic image in Fig. 5C from a keratin antibody (MMAC) stained section from a hyperkeratotic, mildly dysplastic gingiva biopsy with focal moderate to severe dysplasia has 20 – 40 micron heavily keratinized superficial layer a top a 30 – 100 micron thick layer of keratinized cells. This layer is recorded in the plot in Fig. 5D by a brief period of increasing reflected nuclear intensity before the signal varies significantly until 120 microns below the tissue surface. At this depth, the intensity begins to drop. When the data from 120 – 190 microns is fitted to an exponential curve, the fit constant is 69 (with a R^2 value of 0.89), implying a scattering coefficient of 34 cm^{-1} . Figure 6 shows more examples of normalized nuclear reflectance plots from different sites in the oral cavity representing multiple pathologic states. Variations in reflected nuclear intensities in the superficial layer of the measurements are also captured in Figures 6B and 6C. Figure 6 also illustrates an increasing trend in scattering coefficients due to dysplasia and SCC with a hyperkeratotic and hyperplastic biopsy (Figure 6A) having an estimated scattering coefficient of 16 cm^{-1} , a hyperkeratotic, mildly dysplastic biopsy (Figure 6B) having an estimated scattering coefficient of 34 cm^{-1} , a severely hyperkeratotic, moderately dysplastic biopsy (Figure 6C) having an estimated scattering coefficient of 48 cm^{-1} ,

and an invasive, well-differentiated SCC (Figure 6D) having an estimated scattering coefficient of 70 cm^{-1} .

This trend is demonstrated in a scatter plot in Figure 7A for the 20 samples that either did not have a hyperkeratotic region or had a second layer that exhibited an exponential attenuation of reflected nuclear intensity. Figure 7B shows the mean scattering coefficients for these stacks by pathologic diagnosis. The mean scattering coefficient for samples from normal biopsies was $27 \pm 11 \text{ cm}^{-1}$, with a minimum and maximum value of 13 and 42 cm^{-1} , respectively. The mean scattering coefficient for samples from dysplastic biopsies was $39 \pm 6 \text{ cm}^{-1}$, with a minimum and maximum value of 34 and 48 cm^{-1} , respectively. Finally, the mean scattering coefficient for samples from SCC biopsies was $60 \pm 9 \text{ cm}^{-1}$, with a minimum and maximum value of 54 and 70 cm^{-1} , respectively. While the number of samples from SCC is small, there is a increase in the average scattering coefficient as the tissue progresses from normal to dysplasia to cancer.

Discussion

The images presented here illustrate the ability of OCM to image oral mucosa with resolution comparable to histologic evaluation without tissue preparation and staining. In normal tissue, depth-related changes in cell diameter and nuclear density were observed at multiple anatomic sites within the oral cavity. The penetration depth of the OCM was greater than that which could be achieved with confocal microscopy. In SCCs, densely packed, pleomorphic tumor nuclei could be visualized while areas of inflammation appeared dark. Our images correlate well with histology and are similar to previously reported optical imaging results in the oral cavity [12, 29].

Our study of oral epithelial scattering coefficients emphasizes the role that a hyperkeratotic layer plays in optical imaging of the oral cavity. We believe that the low levels of reflected intensity at the superficial portion of the hyperkeratotic layer are due to high levels of keratin that lower the index mismatch between nuclei and the surrounding cytoplasm. The reflected intensity increases as the level of keratin in the cytoplasm drops leading to an increase in refractive mismatch. This result supports the conclusion made in a previous study [29] that a larger refractive index exists in the hyperkeratotic layer that would limit the ability of illumination light to reach lower levels in the tissue by increasing specular reflection at the tissue surface. We also believe that the characteristic depth dependent reflectivities observed in the rest of the hyperkeratotic layer are a result of changing levels of keratin in the cytoplasm as well as pyknotic nuclei. Previous studies have shown that chromatin material in the nucleus is responsible for the index mismatch that provides a significant amount of the contrast in optical imaging of amelanotic tissue [30]. Nuclei present in a hyperkeratotic (or parakeratotic) layer are pyknotic due to the death of cells with condensed, irregular chromatin [31]. Varying shapes and DNA levels would cause the reflectivity and scattering function to fluctuate with each individual nucleus.

The average scattering coefficients reported here show an increase from 27 cm^{-1} in normal tissue to 39 cm^{-1} in dysplastic tissue to 60 cm^{-1} in SCCs. We believe that the increased scattering in abnormal tissue is due to changes in nuclear morphology. Quantitative measures of normal oral epithelium and oral SCC found almost a doubling in DNA content in SCC when compared to normal tissue [32]. Our results are similar to the 22 cm^{-1} and 69 cm^{-1} for normal and dysplastic epithelium, respectively, extracted from cervical tissue confocal images [77] and

the 13 cm^{-1} and 142 cm^{-1} for normal and dysplastic epithelium predicted by our finite difference time domain (FDTD) algorithm which estimated the volume fraction of nuclei and average nuclear size from cervical confocal images [33]. We did observe higher scattering in normal oral mucosa than found in cervical epithelium which we attribute to higher levels of keratin in the cytoplasm.

Recently, a number of studies have suggested that optical spectroscopy and imaging can probe changes in both the epithelium and stroma of both oral and cervical tissue [34-40], but these methods are based on accurate models of the optical properties of the target tissue. Our previous study of cervical epithelial scattering suggested, based on its results for epithelial scattering coefficients, that single layer models that assume tissue is homogeneous are not well suited to describe light propagation in tissue because of the large difference in scattering between epithelium and stroma [27]. Our results further emphasize this point by identifying separate layers within the epithelium with significantly different scattering properties. Therefore, techniques that attempt to accurately model microanatomical and biochemical features of epithelium and their effect on scattering [33, 38, 39, 41] will play a vital role in supporting optical spectroscopy as a tool in the oral cavity.

Conclusion

In this study, we have shown the power of optical coherence microscopy to visualize, at the subcellular level, features of both normal and neoplastic oral mucosa throughout the oral cavity. Penetration depths for the OCM were consistently greater than accompanying confocal imaging. Extraction of scattering coefficients from reflected nuclear intensity was successful in

non-hyperkeratotic layers and showed differentiation between scattering properties of normal and dysplastic epithelium and SCCs.

References

- [1] J. A. Izatt, M. R. Hee, and G. M. Owen, "Optical coherence microscopy in scattering media," *Optics Letters*, vol. 19, pp. 590, 1994.
- [2] J. W. Hettinger, M. de la Pena Mattozzi, W. R. Myers, M. E. Williams, A. Reeves, R. L. Parsons, R. C. Haskell, R. Wang, and J. I. Medford, "Optical coherence microscopy. A technology for rapid, *in vivo*, non-destructive visualization of plants and plant cells," *Plant Physiology*, vol. 123, pp. 3-15, 2000.
- [3] A. Reeves, R. L. Parsons, J. W. Hettinger, and J. I. Medford, "In vivo three-dimensional imaging of plants with optical coherence microscopy," *Journal of microscopy*, vol. 208, pp. 177-89, 2002.
- [4] J. A. Izatt, M. D. Kulkarni, H.-W. Wang, K. Kobayashi, and M. V. Sivak, "Optical coherence tomography and microscopy in gastrointestinal tissues," *IEEE Journal of Selected Topics in Quantum Electronics*, vol. 2, pp. 1017-1028, 1996.
- [5] C. L. Smithpeter, A. K. Dunn, A. J. Welch, and R. Richards-Kortum, "Penetration depth limits of *in vivo* confocal reflectance imaging," *Applied Optics*, vol. 37, pp. 2749-2754, 1998.
- [6] K. J. Busam, K. Hester, C. Charles, D. L. Sachs, C. R. Antonescu, S. Gonzalez, and A. C. Halpern, "Detection of clinically amelanotic malignant melanoma and

assessment of its margins by *in vivo* confocal scanning laser microscopy," *Archives of dermatology*, vol. 137, pp. 923-9, 2001.

- [7] R. G. Langley, M. Rajadhyaksha, P. J. Dwyer, A. J. Sober, T. J. Flotte, and R. R. Anderson, "Confocal scanning laser microscopy of benign and malignant melanocytic skin lesions *in vivo*," *Journal of the American Academy of Dermatology*, vol. 45, pp. 365-76, 2001.
- [8] S. Gonzalez and Z. Tannous, "Real-time, *in vivo* confocal reflectance microscopy of basal cell carcinoma," *Journal of the American Academy of Dermatology*, vol. 47, pp. 869-874, 2002.
- [9] Z. S. Tannous, M. C. Mihm, T. J. Flotte, and S. González, "*In vivo* examination of lentigo maligna and malignant melanoma *in situ*, lentigo maligna type by near-infrared reflectance confocal microscopy: Comparison of *in vivo* confocal images with histologic sections," *Journal of the American Academy of Dermatology*, vol. 46, pp. 260-3, 2002.
- [10] T. Collier, A. Lacy, R. Richards-Kortum, A. Malpica, and M. Follen, "Near real-time confocal microscopy of amelanotic tissue: Detection of dysplasia in *ex vivo* cervical tissue," *Academic Radiology*, vol. 9, pp. 504-512, 2002.
- [11] H. Inoue, T. Igari, T. Nishikage, K. Ami, T. Yoshida, and T. Iwai, "A novel method of virtual histopathology using laser-scanning confocal microscopy *in-vitro* with untreated fresh specimens from the gastrointestinal mucosa," *Endoscopy*, vol. 32, pp. 439-43, 2000.

- [12] W. M. White, M. Rajadhyaksha, S. Gonzalez, R. L. Fabian, and R. R. Anderson, "Noninvasive imaging of human oral mucosa *in vivo* by confocal reflectance microscopy," *Laryngoscope*, vol. 109, pp. 1709-1717, 1999.
- [13] A. Clark, A. M. Gillenwater, T. Collier, R. Alizadeh-Naderi, A. K. El-Naggar, and R. R. Richards-Kortum, "Confocal Microscopy for Real Time Detection of Oral Cavity Neoplasia," *Submitted to Clinical Cancer Research*, 2001.
- [14] W. Drexler, U. Morgner, F. X. Kartner, C. Pitris, S. A. Boppart, X. D. Li, E. P. Ippen, and J. G. Fujimoto, "In vivo ultrahigh-resolution optical coherence tomography," *Optics Letters*, vol. 24, pp. 1221-1223, 1999.
- [15] C. Pitris, A. Goodman, S. A. Boppart, J. J. Libus, J. G. Fujimoto, and M. E. Brezinski, "High-resolution imaging of gynecologic neoplasms using optical coherence tomography," *Obstetrics and gynecology*, vol. 93, pp. 135-9, 1999.
- [16] G. Zuccaro, N. Gladkova, J. Vargo, F. Feldchtein, E. Zagaynova, D. Conwell, G. Falk, J. Goldblum, J. Dumot, J. Ponsky, G. Gelikonov, B. Davros, E. Donchenko, and J. Richter, "Optical coherence tomography of the esophagus and proximal stomach in health and disease," *The American journal of gastroenterology*, vol. 96, pp. 2633-9, 2001.
- [17] S. Jäckle, N. Gladkova, F. Feldchtein, A. Terentieva, B. Brand, G. Gelikonov, V. Gelikonov, A. Sergeev, A. Fritscher-Ravens, J. Freund, U. Seitz, S. Schröder, and N. Soehendra, "In vivo endoscopic optical coherence tomography of esophagitis, Barrett's esophagus, and adenocarcinoma of the esophagus," *Endoscopy*, vol. 32, pp. 750-5, 2000.

- [18] S. Jäckle, N. Gladkova, F. Feldchtein, A. Terentieva, B. Brand, G. Gelikonov, V. Gelikonov, A. Sergeev, A. Fritscher-Ravens, J. Freund, U. Seitz, S. Soehendra, and N. Schröders, "In vivo endoscopic optical coherence tomography of the human gastrointestinal tract--toward optical biopsy," *Endoscopy*, vol. 32, pp. 743-9, 2000.
- [19] A. M. Sergeev, V. M. Gelikonov, G. V. Gelikonov, F. I. Feldchtein, R. V. Kuranov, and N. D. Gladkova, "In vivo endoscopic OCT imaging of precancer and cancer states of human mucosa," *Optics Express*, vol. 1, pp. 432-440, 1997.
- [20] B. E. Bouma, G. J. Tearney, C. C. Compton, and N. S. Nishioka, "High-resolution imaging of the human esophagus and stomach in vivo using optical coherence tomography," *Gastrointestinal endoscopy*, vol. 51(4) Pt 1, pp. 467-74, 2000.
- [21] X. D. Li, S. A. Boppart, J. Van Dam, H. Mashimo, M. Mutinga, W. Drexler, M. Klein, C. Pitris, M. L. Krinsky, M. E. Brezinski, and J. G. Fujimoto, "Optical coherence tomography: advanced technology for the endoscopic imaging of Barrett's esophagus," *Endoscopy*, vol. 32, pp. 921-30, 2000.
- [22] C. A. Jesser, S. A. Boppart, C. Pitris, D. L. Stamper, G. P. Nielsen, M. E. Brezinski, and J. G. Fujimoto, "High resolution imaging of transitional cell carcinoma with optical coherence tomography: Feasibility for the evaluation of bladder pathology," *The British journal of radiology*, vol. 72, pp. 1170-6, 1999.
- [23] B. M. Hoeling, A. D. Fernandez, R. C. Haskell, E. Huang, W. R. Myers, D. C. Peterson, S. E. Ungersma, R. Wang, and M. E. Williams, "An optical coherence microscope for 3-dimensional imaging in developmental biology," *Optics Express*, vol. 6, pp. 136-146, 2000.

- [24] B. M. Hoeling, A. D. Fernandez, R. C. Haskell, and D. C. Petersen, "Phase modulation at 125 kHz in a Michelson interferometer using an inexpensive piezoelectric stack driven at resonance," *Review of Scientific Instruments*, vol. 72, pp. 1630-1633, 2001.
- [25] M. Gu, C. J. R. Sheppard, and X. Gan, "Image formation in a fiber-optical confocal scanning microscope," *Journal of the Optical Society of America A: Optics, Image Science, and Vision*, vol. 8, pp. 1755-1761, 1991.
- [26] R. A. Drezek, T. Collier, C. K. Brookner, A. Malpica, R. Lotan, R. R. Richards-Kortum, and M. Follen, "Laser scanning confocal microscopy of cervical tissue before and after application of acetic acid," *American journal of obstetrics and gynecology*, vol. 182, pp. 1135-9, 2000.
- [27] T. Collier, D. Arifler, R. Richards-Kortum, A. Malpica, and M. Follen, "Determination of epithelial tissue scattering coefficient using confocal microscopy," *IEEE Journal of Selected Topics in Quantum Electronics*, Accepted for Publication.
- [28] J. Qu, C. MacAuley, S. Lam, and B. Palcic, "Optical Properties of normal and carcinomatous bronchial tissue," *Applied Optics*, vol. 33, pp. 7397-7405, 1994.
- [29] A. Clark, A. M. Gillenwater, T. Collier, R. Alizadeh-Naderi, A. K. El-Naggar, and R. R. Richards-Kortum, "Confocal microscopy for real time detection of oral cavity neoplasia," *Clinical Cancer Research*, Accepted for publication.
- [30] C. L. Smithpeter, A. K. Dunn, R. Drezek, T. Collier, and R. Richards-Kortum, "Near real time confocal microscopy of cultured amelanotic cells: Sources of

- signal, contrast agents, and limits of contrast," *Journal of Biomedical Optics*, vol. 3, pp. 429-436, 1998.
- [31] S. L. Robbins, R. S. Cotran, and V. Kumar, *Pathologic Basis of Disease*, 3rd ed. Philadelphia: W. B. Saunders, 1984.
 - [32] Y. Kinoshita, S. Inoue, Y. Honma, and K. Shimura, "Diagnostic significance of nuclear DNA content and nuclear area in oral hyperplasia, dysplasia, and carcinoma," *Journal of oral and maxillofacial surgery*, vol. 50, pp. 728-33, 1992.
 - [33] D. Arifler, M. Guillaud, A. Carraro, A. Malpica, M. Follen, and R. R. Richards-Kortum, "Light Scattering from normal and dysplastic cervical cells at different epithelial depths: finite-difference time-domain modeling with a perfectly matched layer boundary condition," *Journal of Biomedical Optics*, Paper under review.
 - [34] A. Gillenwater, R. Jacob, and R. Richards-Kortum, "Fluorescence spectroscopy: A technique with potential to improve the early detection of aerodigestive tract neoplasia," *Head & Neck*, vol. 20, pp. 556-562, 1998.
 - [35] C. Y. Wang, H. K. Chiang, C. T. Chen, C. P. Chiang, Y. S. Kuo, and S. N. Chow, "Diagnosis of oral cancer by light-induced autofluorescence spectroscopy using double excitation wavelengths," *Oral oncology*, vol. 35, pp. 144-50, 1999.
 - [36] A. Gillenwater, R. Jacob, R. Ganeshappa, B. Kemp, A. K. El-Naggar, J. L. Palmer, G. Clayman, M. F. Mitchell, and R. Richards-Kortum, "Noninvasive diagnosis of oral neoplasia based on fluorescence spectroscopy and native tissue autofluorescence," *Archives of Otolaryngology – Head & Neck Surgery*, vol. 124, pp. 1251-1258, 1998.

- [37] D. C. De Veld, M. Skurichina, M. J. Witjes, R. P. Duin, D. J. Sterenborg, W. M. Star, and J. L. Roodenburg, "Autofluorescence characteristics of healthy oral mucosa at different anatomical sites," *Lasers in surgery and medicine*, vol. 32, pp. 367-76, 2003.
- [38] I. Pavlova, K. Sokolov, R. Drezek, A. Malpica, M. Follen, and R. Richards-Kortum, "Microanatomical and biochemical origins of normal and precancerous cervical autofluorescence using laser-scanning fluorescence confocal microscopy," *Photochemistry and photobiology*, vol. 77, pp. 550-5, 2003.
- [39] R. Drezek, C. Brookner, I. Pavlova, I. Boiko, A. Malpica, R. Lotan, M. Follen, and R. Richards-Kortum, "Autofluorescence microscopy of fresh cervical-tissue sections reveals alterations in tissue biochemistry with dysplasia," *Photochemistry and photobiology*, vol. 73, pp. 636-41, 2001.
- [40] B. Kulapaditharom and V. Boonkitticharoen, "Laser-induced fluorescence imaging in localization of head and neck cancers," *Annals of Otology, Rhinology & Laryngology*, vol. 107, pp. 241-246, 1998.
- [41] R. Drezek, M. Guillaud, T. Collier, I. Boiko, A. Malpica, C. Macaulay, M. Follen, and R. Richards-Kortum, "Light scattering from cervical cells throughout neoplastic progression: influence of nuclear morphology, DNA content, and chromatin texture," *Journal of biomedical optics*, vol. 8, pp. 7-16, 2003.

Table 1. Number of clinically normal and abnormal biopsies from each site.

Location	Clinical Appearance	
	Normal	Abnormal
Tongue (Lateral and Ventral Surfaces)	3	4
Floor of Mouth	2	2
Gingiva	4	6
Buccal Mucosa	3	2
Soft Palate	1	1

Table 2. Histopathologic diagnosis by patient.

#	Site	Histopathologic Diagnosis	
		Clinically Normal Biopsy	Clinically Abnormal Biopsy
1	Tongue (Lat. surface)	Hyperkeratosis, hyperplasia	Moderate focal dysplasia
2	Gingiva	Hyperkeratosis, hyperplasia	Hyperkeratosis, hyperplasia
3	Gingiva	Mild focal dysplasia	Moderate to severe focal dysplasia, hyperkeratosis
4	Gingiva	None ¹	Hyperkeratosis, hyperplasia
5	Soft Palate	Hyperkeratosis, hyperplasia	Well differentiated SCC
6	Floor of mouth (N) ² Gingiva (A) ²	Hyperkeratosis, hyperplasia	None ¹
7	Tongue (Lat. surface)	Hyperkeratosis, hyperplasia	Mild focal dysplasia, hyperkeratosis
8	Floor of mouth	Mild dysplasia, hyperkeratosis	Mild to moderate dysplasia, severe hyperkeratosis
9	Tongue (Lat. surface)	Severe hyperkeratosis, hyperplasia	Mild dysplasia
10	Buccal mucosa (N, A1, A2) ¹	Hyperkeratosis, hyperplasia	Severe hyperkeratosis (A1) Hyperkeratosis, hyperplasia (A2)
11	Buccal mucosa (N) ² Floor of mouth (A1) ² Gingiva (A2) ²	Hyperkeratosis, hyperplasia	Moderate dysplasia, hyperkeratosis (A1) Hyperkeratosis, hyperplasia, (A2)
12	Gingiva	Hyperkeratosis, hyperplasia	Moderately differentiated SCC
13	Buccal mucosa (N) ² Tongue (Lat. surface) (A) ²	Hyperkeratosis, hyperplasia	None ¹

¹No epithelium in specimen.

²The clinically normal (N) and abnormal (A) biopsies were acquired from different sites in the oral cavity due to the extent of the lesion.

Fig. 1. Diagram of the OCM system used to image oral cavity specimens.

Fig. 2. Transverse histologic image (F) with en face confocal (A – E) and OCM (G – K) images obtained at different depths beneath the epithelial surface of a hyperkeratotic and hyperplastic floor of the mouth biopsy. Both imaging modalities captured an increase in nuclear density as the depth of the focal plane increased from (A, G) 50 microns to (B, H) 150 microns to (C, I) 250 microns below the tissue surface. At (D) 300 microns below the tissue surface, confocal image quality started to degrade and by (E) 350 microns below the tissue surface, features were barely resolvable. In the corresponding OCM images, cell membranes (arrow) are still resolvable at (J) 300 microns below the tissue surface. At (K) 350 microns below the tissue surface, cells are captured (arrow) and part of the focal plane has traversed through the basement membrane into stroma (double arrows). Scale bars = 20 microns.

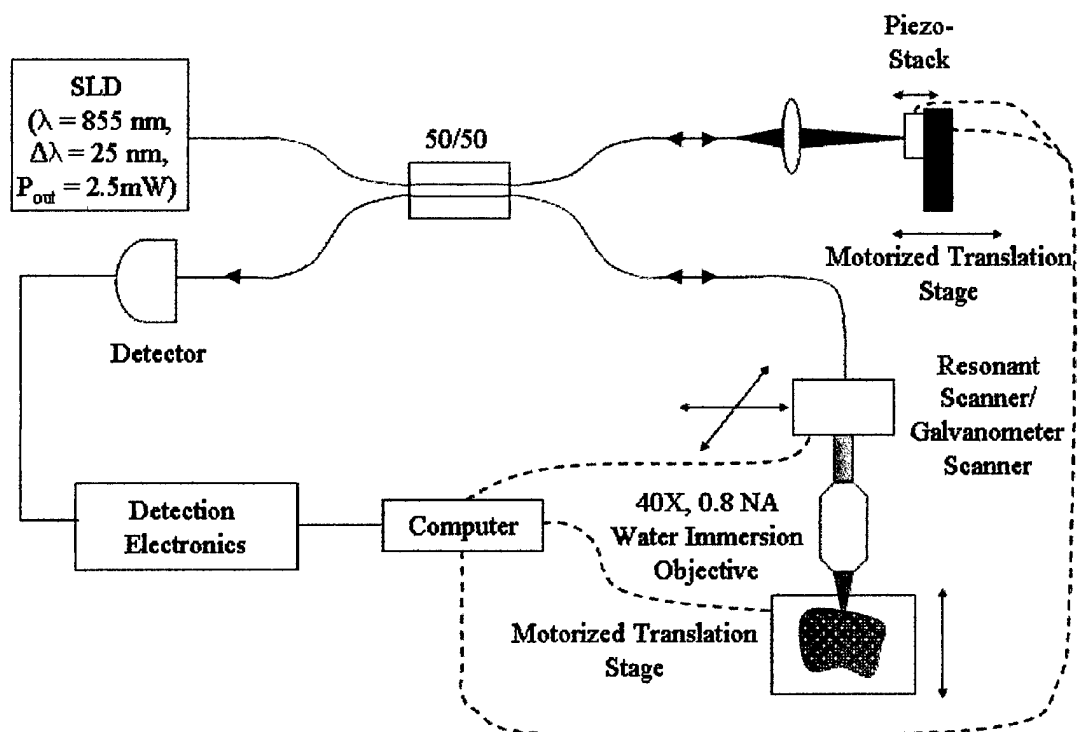
Fig. 3. Histologic and en face OCM images of normal and cancerous tissue. The consistent nuclear area and spacing in images from a hyperplastic and hyperkeratotic biopsy from gingiva (A, C) contrast sharply with the tightly packed tumor cells (arrow) containing irregular nuclei visualized in a well differentiated SCC from the soft palate (B, D). A portion of stroma with inflammation (double arrows) is also captured in both images of the SCC (B, D). Scale bars = 20 microns.

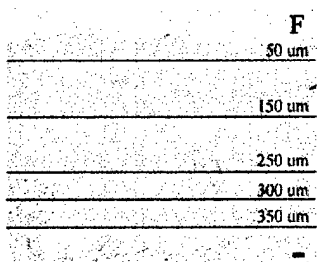
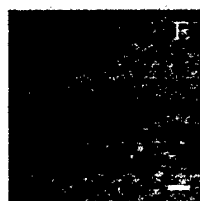
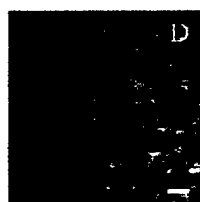
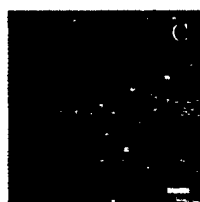
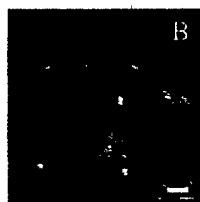
Fig. 4. Penetration depth of confocal microscopy versus OCM system.

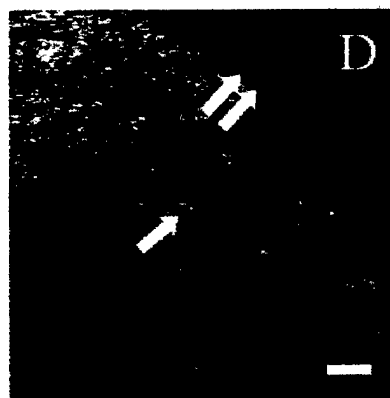
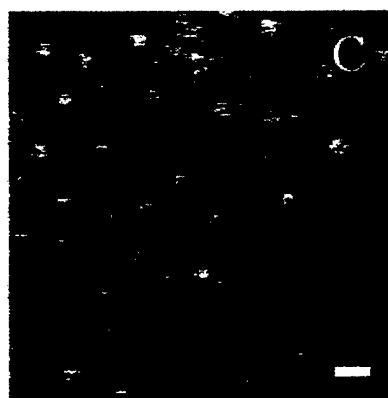
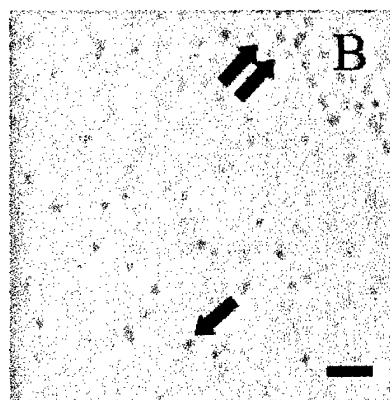
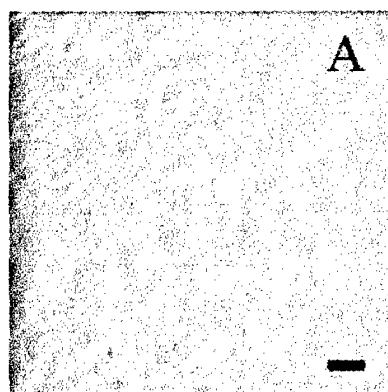
Fig. 5. Comparison of histology to normalized reflected nuclear intensity as a function of depth. (A) Histologic image from a keratin antibody (MMAC) stained section from a hyperkeratotic and hyperplastic gingiva biopsy. (B) Plot of normalized reflected nuclear intensity taken from the same biopsy in (A) showing characteristic decay within the hyperkeratotic region and exponential attenuation starting at 70 microns with a scattering coefficient of 27 cm^{-1} . (C) Histologic image from a keratin antibody (MMAC) stained section from a hyperkeratotic gingiva biopsy with mild dysplasia and focal moderate to severe dysplasia. (D) Plot of normalized reflected nuclear intensity taken from the same biopsy in (C) showing characteristic decay of the hyperkeratotic region and exponential attenuation starting at 120 microns with a scattering coefficient of 34 cm^{-1} .

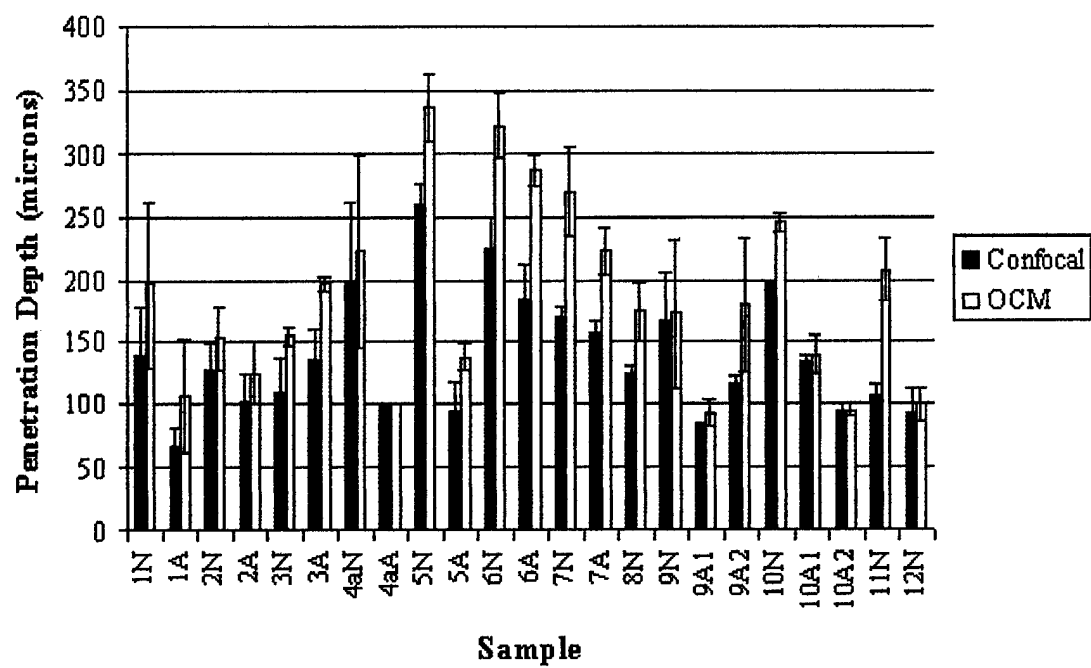
Fig. 6. Examples of normalized nuclear intensity plots from different sites and pathologic states. (A) Plot from a hyperkeratotic and hyperplastic biopsy from the floor of the mouth with an estimated scattering coefficient of 16 cm^{-1} (mean R^2 value of 0.92). (B) Plot from a hyperkeratotic, mildly dysplastic biopsy from the lateral surface of a tongue with an estimated scattering coefficient of 34 cm^{-1} (mean correlation coefficient of 0.96). (C) Plot from a severely hyperkeratotic, moderately dysplastic biopsy from the floor of the mouth with an estimated scattering coefficient of 48 cm^{-1} (mean correlation coefficient of 0.96). (D) Plot from an invasive, well differentiated SCC from the soft palate with an estimated scattering coefficient of 70 cm^{-1} (mean correlation coefficient of 0.98).

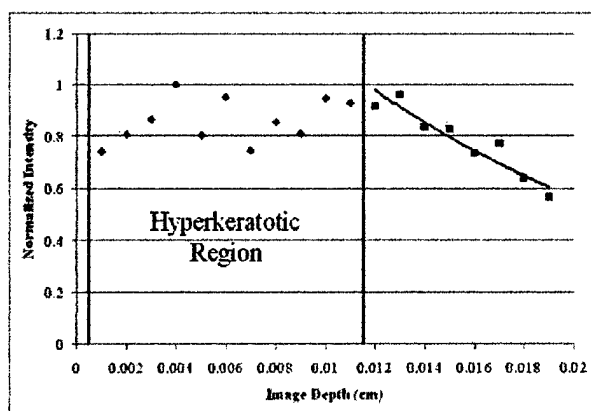
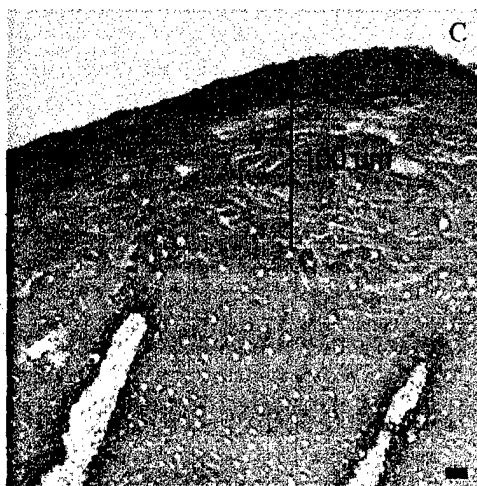
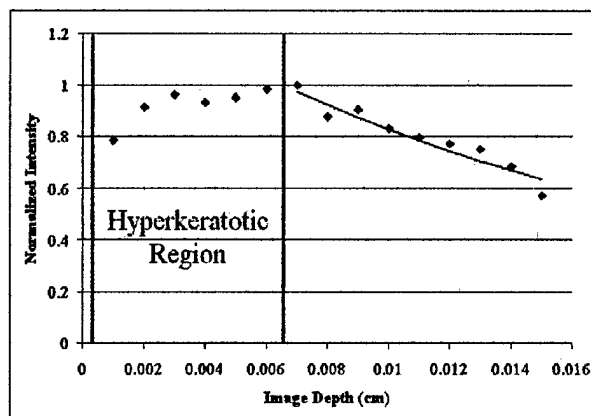
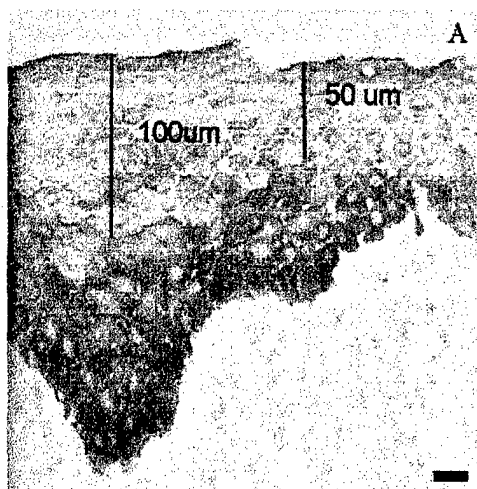
Fig. 7. (a) Scatter plot of scattering coefficients for non-hyperkeratotic tissue. (b) Bar chart comparing mean scattering coefficients for non-hyperkeratotic tissue by pathologic diagnosis.

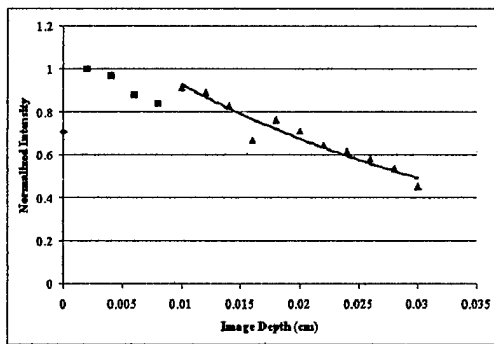




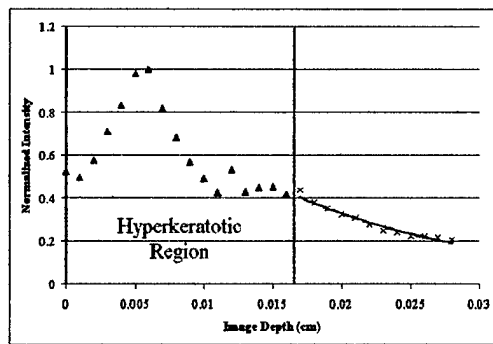




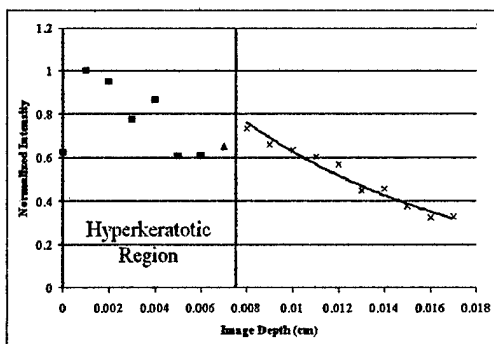




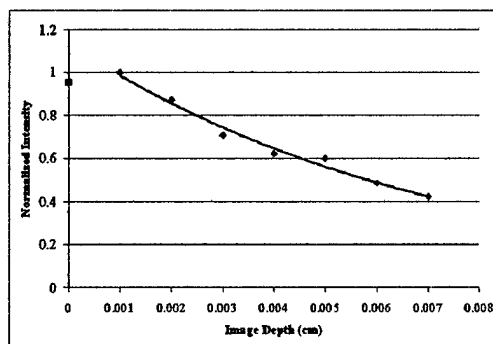
A



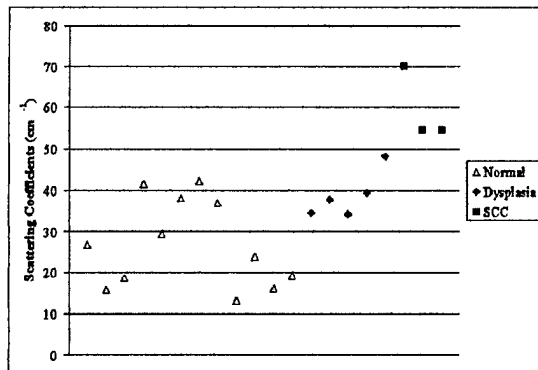
B



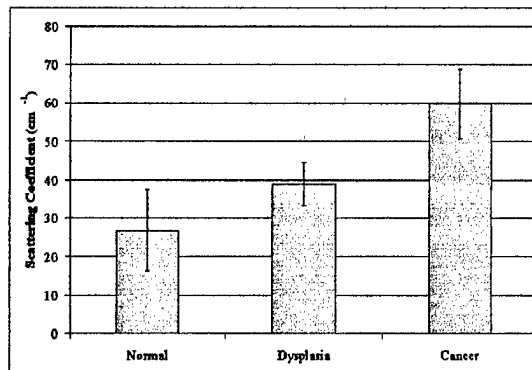
C



D



A



B